Convolution quadrature for the wave equation with impedance boundary conditions

Sauter, Stefan A ; Schanz, Martin

Abstract: We consider the numerical solution of the wave equation with impedance boundary conditions and start from a boundary integral formulation for its discretization. We develop the generalized convolution quadrature (gCQ) to solve the arising acoustic retarded potential integral equation for this impedance problem. For the special case of scattering from a spherical object, we derive representations of analytic solutions which allow to investigate the effect of the impedance coefficient on the acoustic pressure analytically. We have performed systematic numerical experiments to study the convergence rates as well as the sensitivity of the acoustic pressure from the impedance coefficients. Finally, we apply this method to simulate the acoustic pressure in a building with a fairly complicated geometry and to study the influence of the impedance coefficient also in this situation.

DOI: https://doi.org/10.1016/j.jcp.2017.01.013

Convolution Quadrature for the Wave Equation with Impedance Boundary Conditions

S. Sauter* M. Schanz†

August 2016

Abstract

We consider the numerical solution of the wave equation with impedance boundary conditions and start from a boundary integral formulation for its discretization. We develop the generalized convolution quadrature (gCQ) to solve the arising acoustic retarded potential integral equation for this impedance problem.

For the special case of scattering from a spherical object, we derive representations of analytic solutions which allow to investigate the effect of the impedance coefficient on the acoustic pressure analytically. We have performed systematic numerical experiments to study the convergence rates as well as the sensitivity of the acoustic pressure from the impedance coefficients.

Finally, we apply this method to simulate the acoustic pressure in a building with a fairly complicated geometry and to study the influence of the impedance coefficient also in this situation.

1 Introduction

The efficient and reliable simulation of scattered waves in unbounded exterior domains is a numerical challenge and the development of *fast* numerical methods is far from being matured. We are interested in boundary integral formulations of the problem to avoid the use of an artificial boundary with approximate transmission conditions [1, 6, 8, 16, 20] and to allow for recasting the problem (under certain assumptions which will be detailed later) as an integral equation on the surface of the scatterer.

The methods for solving the arising integral equations can be split into a) *frequency domain* methods where an incident plane wave at prescribed frequency excites a scattered field and a time periodic ansatz reduces the problem to a purely spatial Helmholtz equation and b) *time-domain* methods where the excitation is allowed to have a broad temporal band width and, possibly, an a-periodic behavior with respect to time.

For the solution, an ansatz as an acoustic retarded potential integral equation (RPIE) is employed. Among the most popular methods for discretizing this equation are: a) the

*Institut für Mathematik, University Zurich, Winterthurerstrasse 190, CH-8057 Zürich, Switzerland, e-mail: stas@math.uzh.ch

†Institute of Applied Mechanics, Graz University of Technology, 8010 Graz, Austria, e-mail: m.schanz@tugraz.at

convolution quadrature (CQ) method [3, 11, 19, 26–28] and b) the direct *space-time Galerkin discretization* (see, e.g., [2, 17, 18, 36, 38, 40]).

In this paper, the *generalized convolution quadrature* (gCQ) is considered for the discretization of the RPIE. This method has been introduced in [24, 26] for the implicit Euler time method and for the Runge-Kutta method in [25]. In contrast to the original CQ method the gCQ method allows for variable time stepping.

We apply this method to the wave equation with linear impedance boundary condition (for non-linear boundary conditions we refer to [4, 5, 15]) and study the effect of different values of the impedance coefficient on the solution *analytically* for a spherical scatterer and *numerically* for concrete applications with a fairly complicated geometry.

The paper is organized as follows. In Section 2, we will introduce the wave equation with impedance conditions and the corresponding retarded potential integral equation. In Section 3, we introduce the generalized convolution quadrature method for the RPIE with impedance boundary conditions. New representations for analytic solutions in the case of a spherical scatterer are derived in Section 4 which allow for a stable numerical evaluation.

Numerical experiments are described in Section 5. First, systematic studies of the convergence order have been performed for problems where the exact solution is known and the effect of the impedance coefficient on the acoustic pressure is investigated numerically. Then, the method is applied to model the effect of the impedance coefficient for the acoustic pressure in the atrium of the "Institut für Mathematik" at the University Zurich. In 2010/11 an acoustic absorber has been installed at the ceilings to improve the acoustics in the building. Our goal is to model this effect numerically by the gCQ method and the results are also described in Section 5. In the Conclusions 6 we summarize the main findings in this papers.

2 Setting

Let $\Omega^- \subset \mathbb{R}^3$ be a bounded Lipschitz domain with boundary $\Gamma := \partial\Omega$ and let $\Omega^+ := \mathbb{R}^3 \backslash \overline{\Omega^-}$ denote its unbounded complement. Let n denote the unit normal vector to Γ pointing in the exterior domain Ω^+. We consider the homogeneous wave equation (with constant sound speed c in the medium) for $\sigma \in \{+, -\}$

$$\begin{aligned} \partial_{tt} u - c^2 \Delta u &= 0 && \text{in } \Omega^\sigma \times \mathbb{R}_{>0}, \\ u(x,0) = \partial_t u(x,0) &= 0 && \text{in } \Omega^\sigma, \\ \gamma_1^\sigma(u) - \sigma \tfrac{\alpha}{c} \gamma_0^\sigma(\partial_t u) &= f(x,t) && \text{on } \Gamma \times \mathbb{R}_{>0}, \end{aligned} \tag{2.1}$$

where $\gamma_1^\sigma = \partial/\partial n$ is the normal derivative applied to a sufficiently smooth function in Ω^σ and γ_0^σ denotes the trace operator to Γ applied to a sufficiently smooth function in Ω^σ. If the domain $\Omega \in \{\Omega^-, \Omega^+\}$ is clear from the context we skip the superscript σ and simply write γ_1 and γ_0. In (2.1), α denotes the non-negative admittance, which is the inverse of the specific impedance function of the surface Γ. Specific means that the impedance is scaled by the density and the wave velocity. The value of α is mathematically non-negative, however, realistic values are in the range $0 \leq \alpha \leq 1$. The lower limit models a sound hard wall and the upper limit is a totally absorbing surface. Further, measured values show a frequency dependence and are listed in national regulations like the ÖNORM in Austria (ÖNORM EN 12354-6).

Such kind of absorbing boundary condition is a simple possible choice to model the absorption of a surface. Certainly, more complicated models exist which takes higher derivatives

into account. The most realistic models consider an absorbing layer of porous material on the real surface, which is the computational most expensive way (see, e.g., [13, 33]). Here, this simple model is used as it is common in real world applications.

2.1 Layer Potentials

We employ layer potentials to express the solution in terms of retarded potentials (cf. [2, 14, 39, 41]). The ansatz for the solution u as a single layer potential is given by

$$u(x,t) = (\mathcal{S} * \varphi)(x,t) := \int_\Gamma \frac{\varphi\left(y, t - \frac{\|x-y\|}{c}\right)}{4\pi \|x-y\|} d\Gamma_y \qquad \forall (x,t) \in \Omega^\sigma \times \mathbb{R}_{>0},$$

which satisfies the first two equations in (2.1). The density φ then is determined via the third equation. Alternatively we can represent the solution as a double layer potential

$$\begin{aligned} u(x,t) = (\mathcal{D} * \psi)(x,t) &:= \int_\Gamma \left(\frac{\partial}{\partial n(y)} \frac{\psi\left(z, t - \frac{\|x-y\|}{c}\right)}{4\pi \|x-y\|} \right)\Bigg|_{z=y} d\Gamma_y \\ &= \frac{1}{4\pi} \int_\Gamma \frac{\langle n(y), x-y\rangle}{\|x-y\|^2} \left(\frac{\psi\left(y, t - \frac{\|x-y\|}{c}\right)}{\|x-y\|} + \frac{1}{c}\dot{\psi}\left(y, t - \frac{\|x-y\|}{c}\right) \right) d\Gamma_y. \end{aligned}$$

The application of the trace γ_0 and normal trace γ_1 to u involves the following boundary integral operators

$$\begin{aligned} (\mathcal{V} * \varphi)(x,t) &= \int_\Gamma \frac{\varphi\left(y, t - \frac{\|x-y\|}{c}\right)}{4\pi \|x-y\|} d\Gamma_y, \\ (\mathcal{K} * \psi)(x,t) &= \frac{1}{4\pi} \int_\Gamma \frac{\langle n(y), x-y\rangle}{\|x-y\|^2} \left(\frac{\psi\left(y, t - \frac{\|x-y\|}{c}\right)}{\|x-y\|} + \frac{\dot{\psi}\left(y, t - \frac{\|x-y\|}{c}\right)}{c} \right) d\Gamma_y, \\ (\mathcal{K}' * \varphi)(x,t) &= \frac{1}{4\pi} \int_\Gamma \frac{\langle n(x), y-x\rangle}{\|x-y\|^2} \left(\frac{\varphi\left(y, t - \frac{\|x-y\|}{c}\right)}{\|x-y\|} + \frac{\dot{\varphi}\left(y, t - \frac{\|x-y\|}{c}\right)}{c} \right) d\Gamma_y, \\ (\mathcal{W} * \psi)(x,t) &= -\frac{\partial}{\partial n(x)} (\mathcal{D} * \psi)(x,t) \end{aligned}$$

for almost all $(x,t) \in \Gamma \times \mathbb{R}_{>0}$, more precisely, for all $(x,t) \in \Gamma \times \mathbb{R}_{>0}$, where Γ is smooth in a neighborhood of x. Then, it holds for $\sigma \in \{+,-\}$

$$\begin{aligned} \gamma_0^\sigma (\mathcal{S} * \varphi) &= (\mathcal{V} * \varphi), \\ \gamma_1^\sigma (\mathcal{S} * \varphi) &= -\left(\sigma \frac{\varphi}{2} - \mathcal{K}' * \varphi\right), \\ \gamma_0^\sigma (\mathcal{D} * \psi) &= \sigma \frac{\psi}{2} + \mathcal{K} * \psi \\ -\gamma_1^\sigma (\mathcal{D} * \psi) &= \mathcal{W} * \psi, \end{aligned}$$

where, again, these equations hold almost everywhere on $\Gamma \times \mathbb{R}_{>0}$.

The third equation in (2.1) leads to the boundary integral equation for the single layer ansatz

$$-\left(\sigma\frac{\varphi}{2}-\mathcal{K}'*\varphi\right)-\sigma\frac{\alpha}{c}\left(\mathcal{V}*\dot{\varphi}\right)=f \quad \text{a.e. in } \Gamma\times\mathbb{R}_{>0}. \tag{2.2}$$

The double layer ansatz leads to the boundary integral equation

$$-\mathcal{W}*\psi-\frac{\sigma\alpha}{c}\left(\sigma\frac{\dot{\psi}}{2}+\mathcal{K}*\dot{\psi}\right)=f \quad \text{a.e. in } \Gamma\times\mathbb{R}_{>0}. \tag{2.3}$$

3 Generalized Convolution Quadrature (gCQ)

The convolution quadrature method has been developed by Lubich, see [27–31] for parabolic and hyperbolic problems. The idea is to express the RPIE as the inverse Laplace transform applied to the counterpart of the RPIE in the Fourier-Laplace domain which reduces the problem to the solution of a scalar ODE of the form $y'=sy+g$, for s being the variable in the Laplace domain. The temporal discretization then is based on the numerical approximation of the solution of this ODE by some time-stepping method and the transformation of the resulting equation back to the original time domain.

The original CQ method requires constant time stepping. However, if the right-hand side is not uniformly smooth and/or contains non-uniformly distributed variations in time, and/or consists of localized pulses, the use of adaptive time stepping becomes very important in order to keep the number of time steps reasonably small. The *generalized convolution quadrature* (gCQ) has been introduced in [24–26] and allows for variable time stepping.

We recall the definition of the Laplace transform and its inverse

$$\begin{aligned}\hat{f}(s)&:=\mathcal{L}(f)(s):=\int_0^\infty \mathrm{e}^{-st}f(t)\,dt\\ f(t)&:=\frac{1}{2\pi\,\mathrm{i}}\int_\gamma \mathrm{e}^{st}\hat{f}(s)\,ds \quad \text{for } \gamma:=\rho+\mathrm{i}\,\mathbb{R} \text{ and some } \rho>0\end{aligned}$$

for a Laplace-transformable function f, where the vertical contour γ runs from $\rho-\mathrm{i}\,\infty$ to $\rho+\mathrm{i}\,\infty$. The Laplace transformed boundary integral operators are given for sufficiently smooth functions $\Phi,\Psi:\Gamma\to\mathbb{C}$ by (cf. [41], [39])

$$\begin{aligned}
\widehat{\mathcal{S}}(s)\Phi(x)&=\int_\Gamma\frac{\mathrm{e}^{-s\|x-y\|/c}}{4\pi\|x-y\|}\Phi(y)\,d\Gamma_y && \forall x\in\Omega^\sigma \quad \forall s\in\mathbb{C}_\rho,\\
\widehat{\mathcal{D}}(s)\Psi(x)&=\int_\Gamma\frac{\mathrm{e}^{-s\|x-y\|/c}\langle n(y),x-y\rangle}{4\pi\|x-y\|^2}\left(\frac{1}{\|x-y\|}+\frac{s}{c}\right)\Psi(y)\,d\Gamma_y && \forall x\in\Omega^\sigma \quad \forall s\in\mathbb{C}_\rho,\\
\widehat{\mathcal{V}}(s)\Phi(x)&=\int_\Gamma\frac{\mathrm{e}^{-s\|x-y\|/c}}{4\pi\|x-y\|}\Phi(y)\,d\Gamma_y && \forall x\in\Gamma \quad \forall s\in\mathbb{C}_\rho,\\
\widehat{\mathcal{K}}(s)\Psi(x)&=\int_\Gamma\frac{\mathrm{e}^{-s\|x-y\|/c}\langle n(y),x-y\rangle}{4\pi\|x-y\|^2}\left(\frac{1}{\|x-y\|}+\frac{s}{c}\right)\Psi(y)\,d\Gamma_y && \forall x\in\Gamma \quad \forall s\in\mathbb{C}_\rho,\\
\widehat{\mathcal{K}'}(s)\Phi(x)&=\int_\Gamma\frac{\mathrm{e}^{-s\|x-y\|/c}\langle n(x),y-x\rangle}{4\pi\|x-y\|^2}\left(\frac{1}{\|x-y\|}+\frac{s}{c}\right)\Phi(y)\,d\Gamma_y && \forall x\in\Gamma \quad \forall s\in\mathbb{C}_\rho,\\
\widehat{\mathcal{W}}(s)\Psi&=-\frac{\partial}{\partial n(x)}\widehat{\mathcal{D}}(s)\Psi(x) && \forall x\in\Gamma \quad \forall s\in\mathbb{C}_\rho,
\end{aligned}$$

where

$$\mathbb{C}_\rho := \{s \in \mathbb{C} \mid \operatorname{Re} s \geq \rho\} \quad \text{for some } \rho > 0. \tag{3.1}$$

The definition of the (generalized) convolution quadrature depends of the growth behavior of the inverse Laplace transformed integral operator with respect to the frequency variable. This operator must decay fast enough such that the integral over the infinite contour γ exists. In our case this requires a regularization parameter $\mu \in \mathbb{N}_0$ which will be specified later. We denote by $f^{(\mu)}$ as usual the μ-th derivative of f. For $\mu \in \mathbb{Z}$, we define

$$\widehat{\mathcal{V}}_\mu(s) := s^{-\mu}\widehat{\mathcal{V}}(s) \tag{3.2}$$

while $\widehat{\mathcal{K}}_\mu$, $\widehat{\mathcal{K}'}_\mu$, $\widehat{\mathcal{W}}_\mu$ and other frequency dependent integral operators are defined analogously.

The application of the inverse Laplace transform to (2.2) leads to the following integro-differential equation in the frequency domain

$$\frac{1}{2\pi\,\mathrm{i}}\int_\gamma \left(\widehat{Q^\sigma}\right)_{-\mu}(s)\, U(s,t)\, ds = f^{(\mu)}, \tag{3.3a}$$

$$\partial_t U(s,t) = sU(s,t) + \Phi, \qquad U(s,0) = 0, \tag{3.3b}$$

$$\text{with} \quad \widehat{Q^\sigma}(s) := -\left(\frac{\sigma}{2}I - \widehat{\mathcal{K}'}(s)\right) - \sigma\frac{\alpha}{c}s\widehat{\mathcal{V}}(s), \tag{3.3c}$$

where we have suppressed the x-dependence of the functions and operators in the notation.

The same technique can be applied to (2.3) and we obtain

$$\frac{1}{2\pi\,\mathrm{i}}\int_\gamma \left(\widehat{R^\sigma}\right)_{-\mu}(s)\, V(s,t)\, ds = f^{(\mu)} \tag{3.4a}$$

$$\partial_t V(s,t) = sV(s,t) + \Psi, \qquad V(s,0) = 0, \tag{3.4b}$$

$$\text{with} \quad \widehat{R^\sigma}(s) := -\widehat{\mathcal{W}}(s) - \frac{\alpha}{c}s\left(\frac{1}{2}I + \sigma\widehat{\mathcal{K}}(s)\right). \tag{3.4c}$$

The operators $\widehat{Q^\sigma}(s)$ and $\widehat{R^\sigma}(s)$ are continuous and invertible in appropriate Sobolev spaces $H^\mu(\Gamma)$ on the surface Γ and have algebraic growth behavior with respect to $|s|$. Since the growth exponent will be a control parameter for the generalized convolution quadrature, we provide here the relevant theorem.

Theorem 3.1. *Let $\rho > 0$ in (3.1) and $\rho_1 := \min\{1, \rho\}$. Let the admittance function satisfy*

$$0 < \alpha_{\min} := \min_{x\in\Gamma} \alpha(x) \leq \max_{x\in\Gamma} \alpha(x) =: \alpha_{\max} < \infty.$$

Then, the operators $\widehat{Q^\sigma}(s)$ and $\widehat{R^\sigma}(s)$ and their inverses satisfy the following continuity estimates for all $s \in \mathbb{C}_\rho$

$$\left\|\widehat{Q^\sigma}(s)\right\|_{H^{-1/2}(\Gamma)\leftarrow H^{-1/2}(\Gamma)} \leq C_1\left(C_2 + \frac{\alpha_{\max}}{c}\right)|s|^2, \tag{3.5a}$$

$$\left\|\widehat{R^\sigma}(s)\right\|_{H^{-1/2}(\Gamma)\leftarrow H^{1/2}(\Gamma)} \leq C_1\left(C_2 + \frac{\alpha_{\max}}{c}\right)|s|^{5/2}, \tag{3.5b}$$

and

$$\left\|\widehat{Q^\sigma}^{-1}(s)\right\|_{H^{-1/2}(\Gamma)\leftarrow H^{-1/2}(\Gamma)} \leq C_1\frac{c}{\alpha_{\min}}|s|, \tag{3.6a}$$

$$\left\|\widehat{R^\sigma}^{-1}(s)\right\|_{H^{-1/2}(\Gamma)\leftarrow H^{1/2}(\Gamma)} \leq C_2|s|^2. \tag{3.6b}$$

The constants C_1, C_2 only depend on ρ and ρ_1.

Proof. The operator $\widehat{Q^\sigma}(s)$ and $\widehat{R^\sigma}(s)$ can be expressed in terms of the Dirichlet-to-Neumann map DtN^σ and the Neumann-to-Dirichlet map NtD^σ for the exterior ($\sigma = 1$) and the interior ($\sigma = -1$) domain Ω^σ. It holds (cf. [22, Appendix 2])

$$\begin{aligned}\widehat{Q^\sigma}(s) &= -\sigma\left(-\sigma\,\mathrm{DtN}^\sigma + \frac{\alpha}{c}sI\right)\widehat{\mathcal{V}}(s),\\ \widehat{R^\sigma}(s) &= -\left(I - s\frac{\alpha}{c}\sigma\,\mathrm{NtD}^\sigma\right)\widehat{\mathcal{W}}(s).\end{aligned}$$

For the continuity estimates we employ the representations (3.3c) and (3.4c) and well known continuity estimates for $\widehat{\mathcal{K}}$, $\widehat{\mathcal{K}'}$, $\widehat{\mathcal{V}}$, $\widehat{\mathcal{W}}$ (see, e.g., [2, Prop. 3], [12, formulae (10), (11)], [22, Appendix 2]) to obtain

$$\begin{aligned}\left\|\widehat{Q^\sigma}(s)\right\|_{H^{-1/2}(\Gamma)\leftarrow H^{-1/2}(\Gamma)} &\le \frac{1}{2} + C\frac{|s|^{3/2}}{\rho\rho_1^{3/2}} + C\frac{\alpha_{\max}}{c}\frac{|s|^2}{\rho\rho_1^2},\\ \left\|\widehat{R^\sigma}(s)\right\|_{H^{-1/2}(\Gamma)\leftarrow H^{1/2}(\Gamma)} &\le C\frac{|s|^2}{\rho\rho_1} + \frac{\alpha_{\max}}{c}|s|\left(\frac{1}{2} + C\frac{|s|^{3/2}}{\rho\rho_1^{3/2}}\right)\end{aligned}$$

for all $s \in \mathbb{C}_\rho$. From this, estimates (3.5) follow by using $|s| \ge \operatorname{Re} s \ge \rho$.

For the inverses we employ [22, Prop. 17, 18]:

$$\begin{aligned}&\operatorname{Re}\left(\mathrm{e}^{-\mathrm{i}\operatorname{Arg} s}\left(\Phi, \left(-\sigma\,\mathrm{DtN}^\sigma + \frac{\alpha}{c}sI\right)\Phi\right)_{L^2(\Gamma)}\right) \ge \left(C\frac{\rho\rho_1^2}{|s|} + \frac{\alpha_{\min}}{c}|s|\right)\|\Phi\|^2_{H^{1/2}(\Gamma)} \quad \forall \Phi \in H^{1/2}(\Gamma),\\ &\operatorname{Re}\left(\mathrm{e}^{\mathrm{i}\operatorname{Arg} s}\left(\Psi, \left(I - s\frac{\alpha}{c}\sigma\,\mathrm{NtD}^\sigma\right)\Psi\right)_{L^2(\Gamma)}\right) \ge \left(\operatorname{Re} s + C\frac{\alpha_{\min}}{c}\rho\rho_1\right)\frac{1}{|s|}\|\Psi\|^2_{H^{-1/2}(\Gamma)} \quad \forall \Psi \in H^{-1/2}(\Gamma).\end{aligned}$$

The Lax-Milgram lemma implies

$$\begin{aligned}\left\|\left(-\sigma\,\mathrm{DtN}^\sigma + \frac{\alpha}{c}sI\right)^{-1}\right\|_{H^{-1/2}(\Gamma)\leftarrow H^{1/2}(\Gamma)} &\le \frac{|s|}{C\rho\rho_1^2 + \frac{\alpha_{\min}}{c}|s|^2}\\ \left\|\left(I - s\frac{\alpha}{c}\sigma\,\mathrm{NtD}^\sigma\right)^{-1}\right\|_{H^{-1/2}(\Gamma)\leftarrow H^{-1/2}(\Gamma)} &\le \frac{|s|}{C\frac{\alpha_{\min}}{c}\rho\rho_1 + \operatorname{Re} s}.\end{aligned}$$

The combination with well known mapping properties of $\widehat{\mathcal{V}}^{-1}$ and $\widehat{\mathcal{W}}^{-1}$ (cf. [22, Prop. 16, 19]) leads to

$$\begin{aligned}\left\|\widehat{Q^\sigma}^{-1}(s)\right\|_{H^{-1/2}(\Gamma)\leftarrow H^{-1/2}(\Gamma)} &\le \left\|\widehat{\mathcal{V}}^{-1}(s)\right\|_{H^{-1/2}(\Gamma)\leftarrow H^{1/2}(\Gamma)}\left\|\left(-\sigma\,\mathrm{DtN}^\sigma + \frac{\alpha}{c}sI\right)^{-1}\right\|_{H^{-1/2}(\Gamma)\leftarrow H^{1/2}(\Gamma)}\\ &\le C\frac{|s|^2}{\rho\rho_1}\frac{|s|}{C\rho\rho_1^2 + \frac{\alpha_{\min}}{c}|s|^2},\\ \left\|\widehat{R^\sigma}^{-1}(s)\right\|_{H^{-1/2}(\Gamma)\leftarrow H^{1/2}(\Gamma)} &\le \left\|\widehat{\mathcal{W}}^{-1}(s)\right\|_{H^{1/2}(\Gamma)\leftarrow H^{-1/2}(\Gamma)}\left\|\left(I - s\frac{\alpha}{c}\sigma\,\mathrm{NtD}^\sigma\right)^{-1}\right\|_{H^{-1/2}(\Gamma)\leftarrow H^{-1/2}(\Gamma)}\\ &\le C\frac{|s|}{\rho\rho_1^2}\frac{|s|}{C\frac{\alpha_{\min}}{c}\rho\rho_1 + \operatorname{Re} s}\end{aligned}$$

from which the estimates of the inverse operator follow. □

Remark 3.2. *According to the growth of the inverse Laplace transformed integral operators* $\widehat{Q^\sigma}^{-1}(s)$, $\widehat{R^\sigma}^{-1}(s)$ *we define*

$$\mu := \begin{cases} 3 & \text{for problem (2.2),} \\ 4 & \text{for problem (2.3).} \end{cases}$$

This definition implies that the contour integrals $\int_\gamma \left(\widehat{Q^\sigma}^{-1}\right)_\mu (s)\, ds$ *and* $\int_\gamma \left(\widehat{R^\sigma}^{-1}\right)_\mu (s)\, ds$ *exist.*

By approximating the ODE in (3.3b) and (3.4b), by a time stepping scheme and replacing the integral $\int_\gamma \dots$ by a contour quadrature leads to the approximation of (2.2) and (2.3) by generalized convolution quadrature. The following algorithm is taken from [24] and employs the implicit Euler method for discretizing the ODEs in (3.3b), (3.4b); for a generalization to Runge-Kutta methods we refer to [25]. Let time steps $(t_j)_{j=0}^N$ be given

$$0 = t_0 < t_1 < \ldots < t_N = T$$

and introduce the corresponding mesh sizes $\Delta_j = t_j - t_{j-1}$ The implicit Euler method for solving (3.3b) defines approximations $U_n(s) \approx U(s, t_n)$ by

$$U_n = \frac{U_{n-1}}{1 - s\Delta_n} + \frac{\Delta_n \Phi_n}{1 - s\Delta_n}, \qquad U_0 = 0.$$

Inserting this into (3.3a) at time t_n and using Cauchy's integral theorem results in

$$\left(\widehat{Q^\sigma}\right)_{-\mu}\left(\frac{1}{\Delta_n}\right)\Phi_n = f^{(\mu)}(t_n) - \frac{1}{2\pi\,\mathrm{i}}\int_{\mathcal{C}} \frac{\left(\widehat{Q^\sigma}\right)_{-\mu}(s)}{1 - s\Delta_n} U_{n-1}(s)\, ds. \tag{3.7}$$

Here, $\mathcal{C}$ is a bounded contour which encircles all poles $(\Delta_m^{-1})_{m=1}^N$ of the integrand and is clockwise oriented (cf. [24]).

In [23, 24] a quadrature rule for the contour integral in (3.7) has been developed and analyzed. Denote by $s_\ell \in \mathcal{C}$ the nodes and by w_ℓ the weights, $\ell = 1, \cdots, N_Q$. By replacing the integral $\int_{\mathcal{C}} \dots$ by the quadrature formula, we can formulate the generalized convolution quadrature in an algorithmic way.

Definition 3.3 (gCQ)**.** *The generalized convolution quadrature for solving (3.3), (3.4) is given by the procedure: For* $n = 1, \ldots, N$ *do*

$$U_{n-1}(s_\ell) := \left\{ \begin{array}{ll} 0 & n = 1, \\ \frac{U_{n-2}(s_\ell)}{1 - \Delta_{n-1} s_\ell} + \frac{\Delta_{n-1}}{1 - \Delta_{n-1} s_\ell}\Lambda_{n-1} & n \geq 2 \end{array} \right\} \quad \ell = 1, \ldots N_Q \tag{3.8a}$$

$$Z\left(\frac{1}{\Delta_n}\right)\Lambda_n := f^{(\mu)}(t_n) - \sum_{\ell=1}^{N_Q} w_\ell \frac{Z(s_\ell)}{1 - s_\ell \Delta_n} U_{n-1}(s_\ell)\, ds, \tag{3.8b}$$

where $\Lambda_n := \Phi_n$ *and* $Z := \left(\widehat{Q^\sigma}\right)_{-\mu}$ *for problem (3.3) and* $\Lambda_n := \Psi_n$ *and* $Z := \left(\widehat{R^\sigma}\right)_{-\mu}$ *for problem (3.4).*

4 Analytic Solutions

In this section, we provide sample solutions for the wave equation with impedance boundary conditions on the sphere. This allows to study explicitly the influence on the admittance function α on the acoustic pressure and to compare the numerical solution with an exact solution.

There are essentially two different ways for the construction of exact reference solutions for boundary integral equations. One way is to employ Kirchhoff's formulae (see, e.g., [39]) for the wave equation (2.2), (2.3) in the Laplace domain which can be combined such that we get the relations

$$\begin{aligned}\widehat{Q^-}(s)\,\gamma_1^+\widehat{u}^+ &= \widehat{R^-}(s)\,\gamma_0^+\widehat{u}^+,\\ \widehat{Q^+}(s)\,\gamma_1^-\widehat{u}^- &= \widehat{R^+}(s)\,\gamma_0^-\widehat{u}^-\end{aligned}$$

valid for homogeneous interior and exterior solutions u^-, u^+ of the wave equation in the Laplace domain. Such solutions can be created by a source distribution located outside the computational domain

$$u^-(x) := \frac{\mathrm{e}^{-s\|x-y\|/c}}{4\pi\,\|x-y\|} \quad \text{for fixed } y\in\Omega^+ \quad \text{and} \quad u^+(x) := \frac{\mathrm{e}^{-s\|x-y\|/c}}{4\pi\,\|x-y\|} \text{ for fixed } y\in\Omega^-$$

and allow to derive sample solutions for all equations $\widehat{Q^\sigma}(s)\,\Phi = \widehat{f}$ and $\widehat{R^\sigma}(s)\,\Psi = \widehat{f}$, where $\widehat{f}$ is then defined as the application of one of the integral operators $\widehat{Q^\sigma}$, $\widehat{R^\sigma}$ to the trace or normal trace of $\widehat{u}$.

Another approach can be applied for the sphere since the eigenpairs of the boundary integral operator for the acoustic single layer operator are known. From this, we will derive the eigensolutions of the time-space integral equation for the retarded acoustic single layer potential. In this case, the right-hand side is not defined as the application of an integral operator to a trace but known explicitly. In addition, this approach allows to study the behavior of the solution for higher eigenmodes and regularity issues although this study is beyond the scope of this paper. For pure Dirichlet and Neumann problems, such sample solutions have been derived, e.g., in [37] and [42].

Let $\Omega \subset \mathbb{R}^3$ denote the unit ball with surface $\Gamma := \mathbb{S}_2$. Let Y_n^m denote the spherical harmonics. We assume that the right-hand side f is given by

$$f(x,t) := f(t)\,Y_n^m \tag{4.1}$$

with a slight abuse of notation. Note that the spherical harmonics are eigenfunctions of the boundary integral operators $\widehat{\mathcal{V}}, \widehat{\mathcal{K}}, \widehat{\mathcal{K}'}, \widehat{\mathcal{W}}$, i.e.,

$$\widehat{Z}Y_n^m = \lambda_n^{(Z)}\left(\frac{s}{c}\right)Y_n^m \quad \text{for } Z\in\{\mathcal{V},\mathcal{K},\mathcal{K}',\mathcal{W}\}\,.$$

Explicitly it holds (cf. [21, 34])[1]

$$\lambda_n^{(\mathcal{V})}(s) = -s j_n(\mathrm{i}\,s)\, h_n^{(1)}(\mathrm{i}\,s), \qquad \lambda_n^{(\mathcal{K})}(s) = \tfrac{1}{2} - \mathrm{i}\,s^2 j_n(\mathrm{i}\,s)\, \partial h_n^{(1)}(\mathrm{i}\,s),$$

$$\lambda_n^{(\mathcal{W})}(s) = -s^3 \partial j_n(\mathrm{i}\,s)\, \partial h_n^{(1)}(\mathrm{i}\,s), \qquad \lambda_n^{(\mathcal{K}')}(s) = \lambda_n^{(\mathcal{K})}(s),$$

with the spherical Bessel and Hankel functions j_n, $h_n^{(1)}$ (cf. [7, §10.4.7]) and ∂j_n, $\partial h_n^{(1)}$ denoting their first derivatives. Then the Laplace transformed equations (2.2), (2.3) take the form (by using the ansatz $\varphi = \varphi(t)\, Y_n^m$ and $\psi = \psi(t)\, Y_n^m$)

$$\begin{aligned} \widehat{\varphi_n} &= \eta_n^{-1}\left(\alpha, \tfrac{s}{c}\right) \widehat{f}(s) \quad \text{with} \quad \eta_n(\alpha, s) := -\left(\tfrac{\sigma}{2} - \lambda_n^{(\mathcal{K})}(s)\right) - \sigma\alpha s \lambda_n^{(\mathcal{V})}(s), \\ \widehat{\psi_n} &= \gamma_n^{-1}\left(\alpha, \tfrac{s}{c}\right) \widehat{f}(s) \quad \text{with} \quad \gamma_n(\alpha, s) := -\lambda_n^{(\mathcal{W})}(s) - \alpha s \left(\tfrac{1}{2} + \sigma \lambda_n^{(\mathcal{K})}(s)\right). \end{aligned} \tag{4.2}$$

4.1 The Case $n = 0$

For $n = 0$, we have

$$\lambda_0^{(\mathcal{V})}(s) = \tfrac{1-\mathrm{e}^{-2s}}{2s}, \qquad \lambda_0^{(\mathcal{K})}(s) = \tfrac{1}{2} + \tfrac{\mathrm{e}^{-2s}-1}{2s}(s+1)$$

$$\lambda_0^{(\mathcal{W})}(s) = (1+s)\tfrac{s-1+\mathrm{e}^{-2s}(1+s)}{2s}, \qquad \lambda_0^{(\mathcal{K}')}(s) = \lambda_n^{(\mathcal{K})}(s).$$

For the reciprocal symbols η_0^{-1}, γ_0^{-1} we obtain

$$\begin{aligned} \eta_0^{-1}(\alpha, s) &:= -\frac{2s}{\sigma s(1+\alpha) + 1 - \mathrm{e}^{-2s}(s(1+\sigma\alpha)+1)} \\ &= -\frac{2s}{\sigma s(1+\alpha)+1} \sum_{\ell=0}^{\infty} \left(\frac{(s(1+\sigma\alpha)+1)\,\mathrm{e}^{-2s}}{\sigma s(1+\alpha)+1}\right)^{\ell}, \\ \gamma_0^{-1}(\alpha, s) &:= -\frac{2s}{(1+\alpha)s^2 - \sigma\alpha s - 1 + \mathrm{e}^{-2s}(s+1)(s(\sigma\alpha+1)+1)} \\ &= -\frac{2s}{(1+\alpha)s^2 - \sigma\alpha s - 1} \sum_{\ell=0}^{\infty} (-1)^{\ell} \left(\frac{(s+1)((\sigma\alpha+1)s+1)\,\mathrm{e}^{-2s}}{(1+\alpha)s^2 - \sigma\alpha s - 1}\right)^{\ell}. \end{aligned}$$

4.1.1 Single Layer Ansatz, exterior problem

We restrict for the analytic considerations to the exterior problem and to formulation (2.2).

For the exterior problem $\sigma = +1$, we get

$$\eta_0^{-1}(\alpha, s) = -\frac{2s}{s(1+\alpha)+1} \sum_{\ell=0}^{\infty} \mathrm{e}^{-2\ell s}.$$

[1] Note that in [34, (2.6.116)] is a misprint. For the Wronskian $\mathfrak{W}$ of the spherical Bessel functions j_ℓ, $h_\ell^{(1)}$, it holds

$$\mathfrak{W}\left(h_\ell^{(1)}(z), j_\ell(z)\right) = -\frac{\mathrm{i}}{z^2}$$

so that in [34, (3.2.22)] on the right-hand side a factor i is missing. By the same reason a factor i is also missing in the formulae [34, (3.2.23), (3.2.24)], while in formula [34, (3.2.26)] a factor i is missing only in front of the first term in the bracket. Note also that our definition of $\mathcal{W}$ differs from the definition [34, (3.2.17)] by a sign.

The inverse Laplace transform of this function is given by [9, 4.1(4) with $a = 1$ and $b = 2\ell$]

$$\mathcal{L}^{-1}\left(\eta_0^{-1}(\alpha,\bullet)\right)(t) = -\sum_{\ell=0}^{\infty} H(t-2\ell)\,\mathcal{L}^{-1}\left(\frac{2\bullet}{\bullet(1+\alpha)+1}\right)(t-2\ell).$$

We have

$$\mathcal{L}^{-1}\left(\frac{2\bullet}{\bullet(1+\alpha)+1}\right)(t) = \frac{2}{1+\alpha}\mathcal{L}^{-1}\left(1-\frac{1}{1+\alpha}\frac{1}{s+\frac{1}{1+\alpha}}\right)(t) \overset{[9,\ 5.2(1)]}{=} \frac{2}{1+\alpha}\left(\delta_0(t) - \frac{\mathrm{e}^{-\frac{t}{1+\alpha}}}{1+\alpha}\right)$$

with the Dirac delta distribution δ_0 so that

$$\mathcal{L}^{-1}\left(\eta_0^{-1}(\alpha,\bullet)\right)(t) = -\frac{2}{1+\alpha}\sum_{\ell=0}^{\infty} H(t-2\ell)\left(\delta_0(t-2\ell) - \frac{\mathrm{e}^{-\frac{t-2\ell}{1+\alpha}}}{1+\alpha}\right). \tag{4.3}$$

Hence, the density for the single layer ansatz for the exterior problem is given by[2]

$$\varphi^+(t) = -\frac{2}{1+\alpha}\sum_{\ell=0}^{\lfloor ct/2\rfloor}\left(f\left(t-\frac{2\ell}{c}\right) - \frac{c}{1+\alpha}\int_0^{t-2\ell/c}\mathrm{e}^{-\frac{c(t-\tau)-2\ell}{1+\alpha}} f(\tau)\,d\tau\right) \tag{4.4}$$

with the notation $\lfloor x\rfloor$ for the largest integer less than or equal to x.

Example 4.1 (bump functions)**.**

a. ***General bump function.*** *For $\rho > 1$ and $\upsilon > 0$, we choose f in (2.2) as the bump function $f_\upsilon(t) := \left(\frac{c\rho t}{1+\alpha}\right)^\upsilon \mathrm{e}^{-\frac{c\rho t}{1+\alpha}}$. Then, the density in (4.4) can be written in the form*[3]

$$\varphi^+(t) = -\frac{2\rho^\upsilon}{1+\alpha}\sum_{\ell=0}^{\lfloor ct/2\rfloor}\left(\left(\frac{ct-2\ell}{1+\alpha}\right)^\upsilon \mathrm{e}^{-\frac{\rho}{1+\alpha}(ct-2\ell)} - \mathrm{e}^{-\frac{ct-2\ell}{1+\alpha}}\frac{\gamma\left(\upsilon+1,\frac{(\rho-1)}{1+\alpha}(ct-2\ell)\right)}{(\rho-1)^{\upsilon+1}}\right). \tag{4.6}$$

b. *For $f_\upsilon(t) = (ct)^\upsilon \mathrm{e}^{-ct}$ it holds*

$$\varphi^+(t) = -\frac{2}{1+\alpha}\sum_{\ell=0}^{\lfloor ct/2\rfloor}\left((ct-2\ell)^\upsilon \mathrm{e}^{-(ct-2\ell)} - \frac{(1+\alpha)^\upsilon}{\alpha^{\upsilon+1}}\gamma\left(\upsilon+1,\frac{\alpha}{1+\alpha}(ct-2\ell)\right)\mathrm{e}^{-\frac{ct-2\ell}{1+\alpha}}\right). \tag{4.7}$$

[2]Let $\kappa > 0$. Then $\mathcal{L}^{-1}\left(\hat{f}\left(\frac{\cdot}{\kappa}\right)\right)(t) = \kappa\left(\mathcal{L}^{-1}(f)\right)(\kappa t)$ (see [9, 4.1(4) with $a = \kappa$, $b = 0$.]). Also note that $\int_{\mathbb{R}}\delta_0(\kappa t - a) = \frac{1}{\kappa}\delta_0\left(\frac{a}{\kappa}\right)$.

[3]For $r > 0$, $\mu > 0$, $\beta \in \mathbb{R}$ it holds

$$\int_0^r s^\mu \mathrm{e}^{-\beta s}\,ds = \frac{\gamma(\mu+1, r\beta)}{\beta^{\mu+1}}, \tag{4.5}$$

where

$$\gamma(a,z) := \int_0^z t^{a-1}e^{-t}dt$$

is an incomplete Gamma function (cf. [7, 8.2.1]).

4.2 The Solution of the Wave Equation in Ω^σ

The Laplace transformed solution of the boundary integral equation for the single layer operator (4.2) with right-hand side as in (4.1) is given by

$$\widehat{\varphi}_n(x,s) := \eta_n^{-1}\left(\alpha, \frac{s}{c}\right)\widehat{f}(s)\, Y_n^m(x).$$

This leads to the solution of the interior and exterior Laplace transformed wave equation (2.1)

$$\widehat{u}^\sigma(x,s) = \widehat{\mathcal{S}}(s)\,\widehat{\varphi}_n(x,s) := \eta_n^{-1}\left(\alpha, \frac{s}{c}\right)\widehat{f}(s)\int_\Gamma \frac{\mathrm{e}^{-s\|x-y\|/c}}{4\pi\,\|x-y\|} Y_n^m d\Gamma_y \qquad \forall\,(x,t)\in\Omega^\sigma\times\mathbb{R}_{>0}$$

and we have to evaluate the application of the Laplace transformed single layer potential to the spherical harmonics Y_n^m. Let

$$\widehat{U}_n^m := \widehat{\mathcal{S}}(s)\, Y_n^m.$$

Then $\widehat{U}_n^m$ satisfies the transmission problem

$$\begin{aligned}
-\Delta\widehat{U}_n^m + \left(\frac{s}{c}\right)^2\widehat{U}_n^m &= 0 \qquad \text{in } \mathbb{R}^3\backslash\Gamma,\\
\left[\gamma_0\widehat{U}_n^m\right]_\Gamma &= 0\\
\left[\gamma_1\widehat{U}_n^m\right]_\Gamma &= -Y_n^m\\
\left|\frac{\partial\widehat{U}_n^m}{\partial r} + \frac{s}{c}\widehat{U}_n^m\right| &= o\left(\|\mathbf{x}\|^{-1}\right) \quad \|\mathbf{x}\|\to\infty.
\end{aligned}$$

From [34, (2.6.53), (2.6.55)] we conclude that the solution in spherical coordinates $x = r\boldsymbol{\zeta}$ has the form

$$\widehat{U}_n^m(x,s) = Y_n^m(\boldsymbol{\zeta})\begin{cases}\beta_n^-(s)\, j_n(\mathrm{i}\,sr) & 0\le r<1\\ \beta_n^+(s)\, h_n^{(1)}(\mathrm{i}\,sr) & r>1\end{cases}$$

with coefficients $\beta_n^\pm$ to be determined via the transmission conditions:

$$\beta_n^-(s)\, j_n(\mathrm{i}\,s) = \beta_n^+(s)\, h_n^{(1)}(\mathrm{i}\,s) \quad \text{and} \quad \mathrm{i}\,s\beta_n^-(s)\, j_n'(\mathrm{i}\,s) - \mathrm{i}\,s\beta_n^+(s)\left(h_n^{(1)}\right)'(\mathrm{i}\,s) = 1.$$

By solving this for $\beta_n^\pm$ we end up with

$$\widehat{U}_n^m(x,s) = \rho_n\left(\frac{s}{c}, r\right) Y_n^m(\boldsymbol{\zeta}) \quad \text{with} \quad \rho_n(s,r) := -s\begin{cases} h_n^{(1)}(\mathrm{i}\,s)\, j_n(\mathrm{i}\,sr) & 0\le r\le 1,\\ j_n(\mathrm{i}\,s)\, h_n^{(1)}(\mathrm{i}\,sr) & 1\le r.\end{cases}$$

This leads to

$$\widehat{u}^\sigma(x,s) = \eta_n^{-1}\left(\alpha, \frac{s}{c}\right)\widehat{f}(s)\,\rho_n\left(\frac{s}{c}, r\right) Y_n^m(\boldsymbol{\zeta}) \qquad \forall\,(r\boldsymbol{\zeta},t)\in\Omega^\sigma\times\mathbb{R}_{>0}$$

For $n = m = 0$, we get

$$\rho_0(s,r) := \frac{\mathrm{e}^{-s|r-1|} - \mathrm{e}^{-s(r+1)}}{2sr}$$

so that

$$\widehat{u}^\sigma(x,s) = q_0\left(\alpha, \frac{s}{c}, r\right)\widehat{f}(s)\, Y_0^0$$

with

$$q_0(\alpha,s,r) := \frac{\rho_0(s,r)}{\eta_0(\alpha,s)} = -\frac{1}{r}\frac{\mathrm{e}^{-s|r-1|} - \mathrm{e}^{-s(r+1)}}{\sigma s(1+\alpha)+1}\sum_{\ell=0}^{\infty}\left(\frac{(s(1+\sigma\alpha)+1)\,\mathrm{e}^{-2s}}{\sigma s(1+\alpha)+1}\right)^\ell.$$

4.2.1 The Solution of the Wave Equation in Ω^+

For $\sigma = +1$, we get

$$q_0(\alpha, s, r) = -\frac{1}{r}\frac{1}{s(1+\alpha)+1}\sum_{\ell=0}^{\infty}\left(\mathrm{e}^{-s(2\ell+r-1)} - \mathrm{e}^{-s(2\ell+r+1)}\right).$$

The inverse Laplace transform applied to $\widehat{u}^+$ can be computed by similar techniques as used for (4.3)

$$\begin{aligned}\mathcal{L}^{-1}\left(q_0(\alpha, \bullet, r)\right)(t) = -\frac{1}{r}\frac{1}{1+\alpha}\sum_{\ell=0}^{\infty}\Big(&H\left(t-(2\ell+r-1)\right)\mathrm{e}^{-\frac{t-(2\ell+r-1)}{1+\alpha}} \\ &-H\left(t-(2\ell+r+1)\right)\mathrm{e}^{-\frac{t-(2\ell+r+1)}{1+\alpha}}\Big)\end{aligned}$$

and the exterior solution u^+ finally is given by

$$\begin{aligned}u^+(r\boldsymbol{\zeta}, t) &= -\frac{c}{2\sqrt{\pi}(1+\alpha)r}\left(\sum_{\ell=0}^{\left\lfloor\frac{ct-r+1}{2}\right\rfloor}\int_0^{t-\frac{2\ell+r-1}{c}}\mathrm{e}^{-\frac{c(t-\tau)-(2\ell+r-1)}{1+\alpha}}f(\tau)\,d\tau\right. \\ &\quad\left.-\sum_{\ell=0}^{\left\lfloor\frac{ct-r-1}{2}\right\rfloor}\int_0^{t-\frac{2\ell+r+1}{c}}\mathrm{e}^{-\frac{c(t-\tau)-(2\ell+r+1)}{1+\alpha}}f(\tau)\,d\tau\right) \\ &= -\frac{c}{2\sqrt{\pi}(1+\alpha)r}\,\mathrm{e}^{-\frac{ct-r+1}{1+\alpha}}\int_0^{t-\frac{r-1}{c}}\mathrm{e}^{\frac{c\tau}{1+\alpha}}f(\tau)\,d\tau, \qquad (4.8)\end{aligned}$$

where we used $Y_0^0 = (2\sqrt{\pi})^{-1}$.

Example 4.2 (bump functions (revisted))**.** *Let $f_\upsilon(t)$ be the general bump function as in Example 4.1 and, for $r > 1$, we define $\tau := ct - (r-1)$. Let $(\tau)_+ := \max\{0, \tau\}$. Then*

$$u^+(r\boldsymbol{\zeta}, t) = -\frac{\rho^\upsilon}{2\sqrt{\pi}(\rho-1)^{\upsilon+1}}\gamma\left(\upsilon+1, \frac{\rho-1}{1+\alpha}\tau_+\right)\frac{\mathrm{e}^{-\frac{\tau}{1+\alpha}}}{r}$$

For $f(t) = (ct)^\upsilon\,\mathrm{e}^{-ct}$ the representation of u^+ simplifies to

$$u^+(r\boldsymbol{\zeta}, t) = -\frac{(1+\alpha)^\upsilon}{2\sqrt{\pi}\alpha^{\upsilon+1}}\gamma\left(\upsilon+1, \frac{\alpha}{1+\alpha}\tau_+\right)\frac{\mathrm{e}^{-\frac{\tau}{1+\alpha}}}{r}. \qquad (4.9)$$

The dependence of $u^+(r\boldsymbol{\zeta}, t)$ with respect to $\alpha \geq 0$ is smooth. For $r \geq 1$, it holds

$$\left|u^+(r\boldsymbol{\zeta}, t)\right| \leq \frac{1}{\sqrt{\pi}(\upsilon+1)(1+\alpha)}\frac{(\tau)_+^{\upsilon+1}}{1+\frac{\alpha}{1+\alpha}\tau}\frac{\mathrm{e}^{-\frac{\tau}{1+\alpha}}}{r}.$$

With increasing α the amplitude of the acoustic pressure is damped by $\frac{1}{1+\alpha}$ and the same holds for the exponent which determines the reverberation time.

Proof. By using (4.8) and the definition of f_υ we get

$$u^+(r\boldsymbol{\zeta},t) = -\frac{c}{2\sqrt{\pi}\,(1+\alpha)\,r}\,\mathrm{e}^{-\frac{ct-r+1}{1+\alpha}}\int_0^{t-\frac{r-1}{c}}\mathrm{e}^{-\frac{c(\rho-1)\tau}{1+\alpha}}\left(\frac{c\rho\tau}{1+\alpha}\right)^{\upsilon}d\tau.$$

1st Case: $ct \le r-1$.
Obviously $u^+ = 0$ in this case.
2nd Case: $r-1 < ct$**.** We employ (4.5) and obtain

$$u^+(x,t) = -\frac{\rho^\upsilon}{(\rho-1)^{\upsilon+1}}\,\mathrm{e}^{-\frac{ct-r+1}{1+\alpha}}\,\frac{\gamma\left(\upsilon+1,(\rho-1)\,\frac{ct-r+1}{1+\alpha}\right)}{2\sqrt{\pi}r}. \tag{4.10}$$

Next we set $\rho = 1+\alpha$ so that the right-hand side becomes $f(t) = (ct)^\upsilon\,\mathrm{e}^{-ct}$ and we obtain

$$u^+(r\boldsymbol{\zeta},t) = \begin{cases} 0 & t \le \frac{r-1}{c}, \\ -\frac{(1+\alpha)^\upsilon}{\alpha^{\upsilon+1}}\frac{\gamma\left(\upsilon+1,\frac{\alpha}{1+\alpha}(ct-r+1)\right)}{2\sqrt{\pi}r}\,\mathrm{e}^{-\frac{ct-r+1}{1+\alpha}} & t > \frac{r-1}{c}. \end{cases}$$

From [7, 8.10.2 with $a>1$ therein] we conclude that for $a \ge 1$ and $x \ge 0$ it holds

$$|\gamma(a,x)| \le \frac{x^{a-1}}{a}\left(1-e^{-x}\right) \le \frac{2x^a}{a\,(x+1)}.$$

For $\tau = ct-(r-1)$ and $r>1$, we have

$$\left|u^+(r\boldsymbol{\zeta},t)\right| \le \frac{1}{\sqrt{\pi}\,(\upsilon+1)\,(1+\alpha)}\,\frac{(\tau)_+^{\upsilon+1}}{1+\frac{\alpha}{1+\alpha}\tau}\,\frac{\mathrm{e}^{-\frac{\tau}{1+\alpha}}}{r}.$$

□

5 Numerical Experiments

The purpose of this Section is to show a) how the proposed algorithm performs for model problems and b) its applicability to real-world problems. For the first goal, a systematic convergence study is presented, which utilizes the analytical solution for the sphere from Section 4. To show the applicability for real-world applications we computed the sound pressure field in the atrium of the "Institut für Mathematik" at the University Zurich with gCQ and the influence of sound absorbing material.

All computations are done in 3-D and a classical matrix-oriented spatial boundary element discretization is employed for a systematic study of the behavior of the gCQ. All regular integrals are performed with Gaussian quadrature formulas. The singular integrals are treated with the formulas as in [10]. The geometrical discretization is done with linear triangles and the data are approximated by piecewise linear shape functions. For the solution a direct solver is used. All implementations are done within the BE-library HyENA [32].

5.1 Unit sphere: Convergence and influence of α

The geometry chosen is a sphere with radius 1 m with a coordinate system fixed at the midpoint. The scattering into the outer air is considered and the respective analytical solutions

can be found in Section 4. For the spherical harmonics in the right-hand side the case of (4.1), we choose $n = m = 0$. The time behavior of the right-hand side is the discussed bump function

$$f_\upsilon(t) = (ct)^\upsilon \, \mathrm{e}^{-ct} \,,$$

with $\upsilon > 0$, i.e., the analytical solutions can be found in (4.7) for the density and in (4.9) for the pressure. For all tests the material data from air are used, i.e., $c = 343\,\mathrm{m/s}$ is set. In contrast to the classical CQ method, the gCQ method allows for a variable step size which becomes important to approximate solutions with singular behavior, e.g., at the initial or later times. Note that for $\upsilon \in \mathbb{R}_{>0} \backslash \mathbb{N}$ the bump function f_υ is Hölder continuous, more precisely $f_\upsilon \in C^{\lfloor \upsilon \rfloor, \{\upsilon\}}$ with $\lfloor \upsilon \rfloor$ denoting the integer part of υ and $\{\upsilon\} := \upsilon - \lfloor \upsilon \rfloor$. From (4.7) it follows that the non-smooth behavior of f_υ at $t = 0$ inherits qualitatively the same order of non-smoothness to the density function at time points $t_\ell = 2\ell/c$, $\ell \in \mathbb{N}_0$, i.e., $\varphi^+ \in C^{\lfloor \upsilon \rfloor, \{\upsilon\}}$. Since u_+ is defined via an integration (involved in the gamma function γ, see (4.9)) we conclude that $u_+ \in C^{\lfloor \upsilon \rfloor + 1, \{\upsilon\}}$.

For simplicity, we assume $\upsilon \in (0, 1)$. If we want to distribute N time points in the interval $[0, T]$ such that a piecewise constant interpolation converges as $\mathcal{O}(N^{-1})$, the choice

$$t_n = T \left(\frac{n}{N} \right)^\chi, \; n = 0, \ldots, N \quad \text{with grading exponent} \quad \chi = 1/\upsilon \tag{5.1}$$

of the mesh points is recommended. Since we employ the BDF 1 method for the time discretization we expect an error in the approximation of the density function of $\mathcal{O}(\Delta t_{\text{const}})$ for $\Delta t_{\text{const}} = T/N$. For a uniform mesh with $t_n = n \Delta t_{\text{const}}$ we expect a reduced convergence order of $\mathcal{O}((\Delta t_{\text{const}})^\upsilon)$. To achieve a comparable error of $\mathcal{O}(N^{-1})$ for a constant mesh width one has to choose a constant time mesh with step size $\Delta t_{\min} = \mathcal{O}\left(N^{-1/\upsilon}\right)$ where $1/\upsilon > 1$.

The error compared to the analytical solution is measured only in time as the spatial behavior of the solution is constant due to the geometry and loading. As an error measure, we employ a discrete L^2-error by integrating numerically over the time with a trapzoidal rule. This results in

$$\begin{aligned} \mathrm{err}_{\text{abs}} &= \sqrt{\sum_{n=0}^{N} \Delta t_n \left(u(t_n) - u_h(t_n) \right)^2} \\ \mathrm{err}_{\text{rel}} &= \mathrm{err}_{\text{abs}} \left(\sum_{n=0}^{N} \Delta t_n \left(u(t_n) \right)^2 \right)^{-\frac{1}{2}} \,, \end{aligned} \tag{5.2}$$

evaluated at some arbitrary point on the surface for the density and at $x = (1.5, 0, 0)^\intercal$ for the pressure field. The index $()_h$ indicates the boundary element solution, whereas the other quantity is the respective exact solution. The order of the numerical convergence (eoc) is defined with

$$\mathrm{eoc} = \log_2 \left(\frac{\mathrm{err}_h}{\mathrm{err}_{h+1}} \right) \,, \tag{5.3}$$

where the indices $()_{h+1}$ and $()_h$ denotes two subsequent refinement levels.

For the following tests four different meshes of the sphere are used (see Fig. 1). The triangles are uniformly refined by subdividing from mesh 1 to mesh 4. The corresponding data as element, node numbers, and respective characteristic element size h are given in Tab. 1. Note that the values of Δt_{const} and h are rounded while, for the computations, more

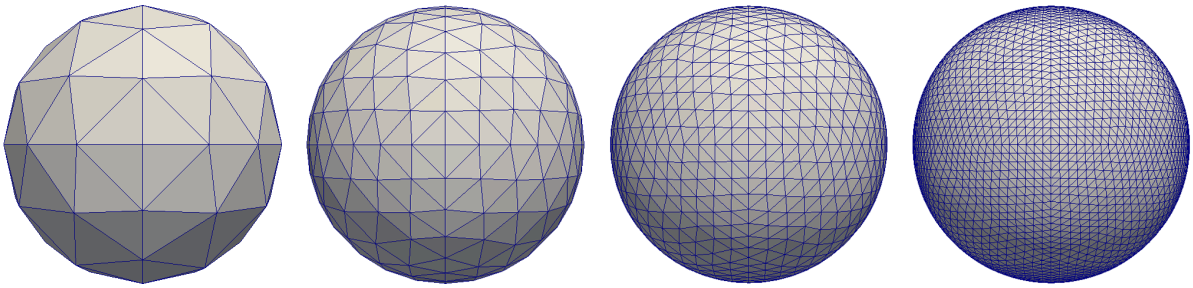

(a) mesh 1 (b) mesh 2 (c) mesh 3 (d) mesh 4

Figure 1: Spatial discretisations for the sphere

	Number		h	$\beta = 0.25$		$\beta = 0.125$		$\beta = 0.0625$	
	elements	nodes		Δt_{const}	N	Δt_{const}	N	Δt_{const}	N
mesh 1	128	66	0.393 m	0.000286	11	0.000143	21	0.000072	41
mesh 2	512	258	0.196 m	0.000143	21	0.000072	41	0.000036	82
mesh 3	2048	1026	0.098 m	0.000072	41	0.000036	82	0.000018	163
mesh 4	8192	4098	0.049 m	0.000036	82	0.000018	163	0.000009	270

Table 1: Data of the refined meshes ($\beta = {}^{c\Delta t_{const}}/_{h}$)

digits are used. Mesh 1 consists of 16 elements on a great circle of the sphere. Based on this number the values of Δt_{const} are computed. To characterize the relation between the spatial and temporal mesh the dimensionless parameter $\beta = {}^{c\Delta t_{const}}/_{h}$ is introduced and also given in Tab. 1. The chosen data result in an observation period up to $T = 0.002915905\,\text{s}$, which is approximately the inverse of the wave speed. It must be remarked that for mesh 4 the smallest time step size would have required $N = 326$ but that many time steps can not be computed on the available hardware. In the following tests, the value $\upsilon = 1/2$ is set for the bump function, which fits to the grading parameter $\chi = 2$. In this setting the smallest step size is approximately the square of the largest step size.

The first study keeps the value of β constant, hence a refinement in space yields a refinement in the temporal variable as well. The admittance is set to $\alpha = 0.5$. The relative error of the density function is plotted in Fig. 2 versus the spatial discretization. To have a comparison, the expected eoc = 1 is given with a dash-dotted line and eoc = 0.5 with a dotted line. The results show that the method converges with the expected rates. Obviously, the constant time step produces a smaller error but has a smaller convergence order compared to the graded time mesh. Since the pressure is more regular as the density (as explained in the beginning of this section), a better behavior for constant step sizes can be expected. This is somehow confirmed by the results for the pressure. These errors are given in Fig. 3 also versus the spatial discretisation. These solutions of the wave equation are fitting well the expected eoc = 1 also for the constant time mesh and both time meshes behave similar. Apparently, there is one exceptional point for $\Delta t_{var}, \beta = 0.0625$. The value for the finest spatial mesh increases slightly. This might be explained by the non-consistent choices of parameters due to hardware limitation. As already stated, for mesh 4 with $\beta = 0.0625$ the number of time steps to arrive at the final time T is too large for the computer memory since all matrices have to be stored for the gCQ method - in contrast to the original CQ method. We expect that this bottleneck can be cured by developing fast versions of gCQ as a topic of future research.

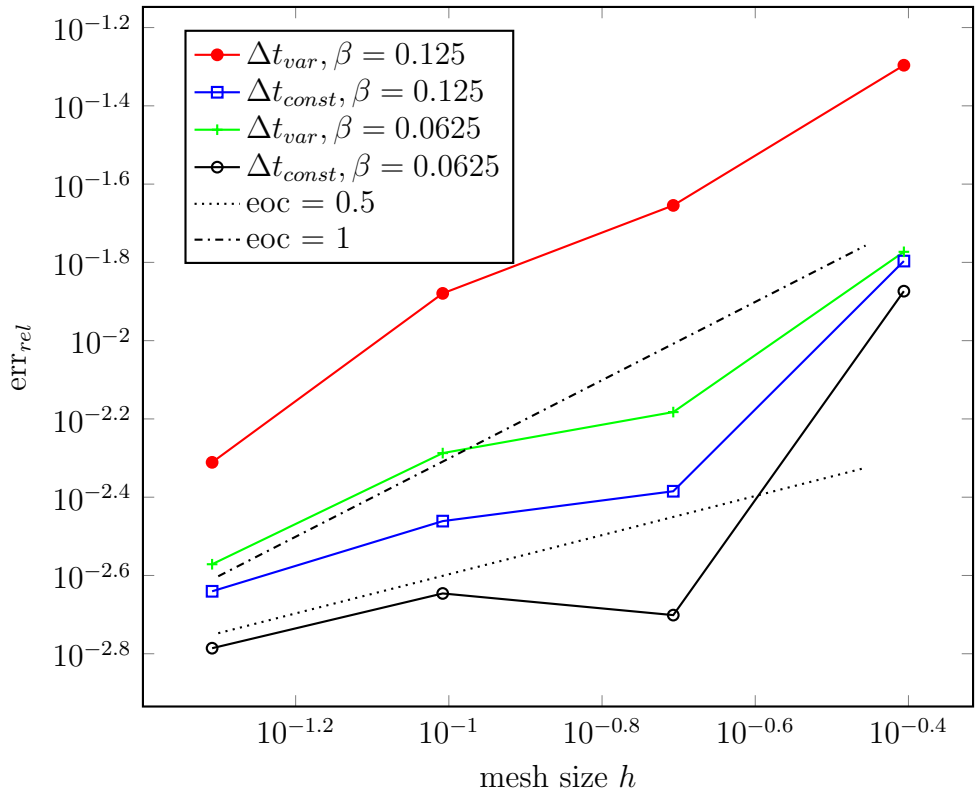

Figure 2: Relative error of the density for different meshes (double logarithmic scale)

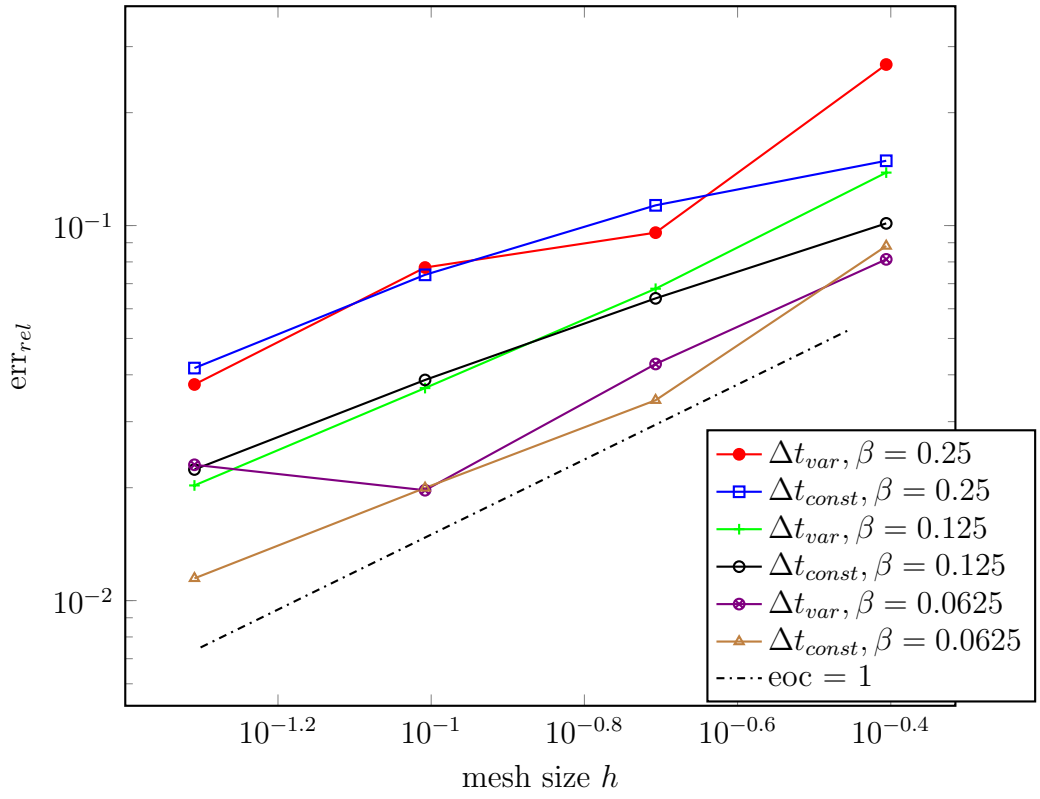

Figure 3: Relative error of the pressure for different meshes (double logarithmic scale)

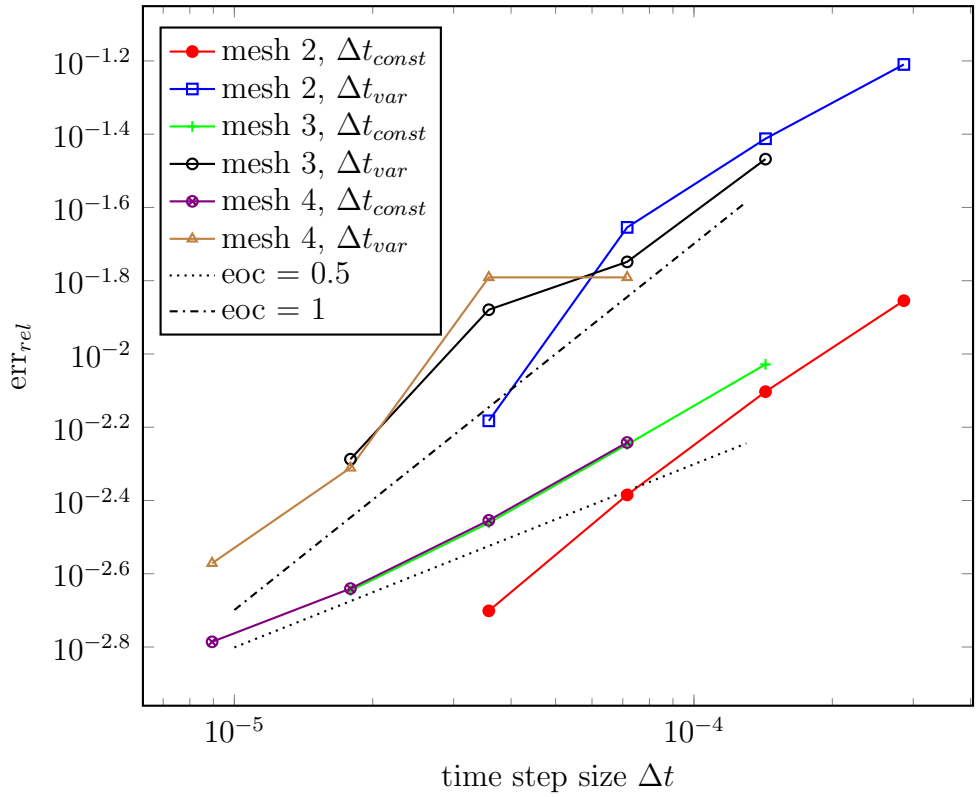

Figure 4: Relative error of the density versus time step size for the different meshes (double logarithmic scale)

Hence, we have fixed the number of time steps for gCQ to $N = 270$ while, for CQ, we have chosen $N = 326$. It seems that this shorter observation period deteriorates the error. It must be remarked that the error of the density does not show this behavior.

Another view on the convergence behavior is to keep the spatial discretization constant and refine only in time. Such a test setting may be not recommended in space-time methods as the spatial and temporal behavior of the results are coupled. But in the special setting of this example the spatial result is a constant value and, hence, independent on the spatial mesh. This can also be observed in the results as they are independent on the chosen spatial point on the surface. Therefore, it is possible to study only the quality of the temporal discretization. For this test the time grading is set again to $\chi = 2$. In Fig. 4, the relative error of the density is given versus the time step size for different meshes. In addition two eocs are plotted with dashed or dotted lines. They show the expected convergence rates in time as discussed in the beginning of this section. The linear convergence of the graded mesh drops to eoc = 0.5 if a constant time mesh is used. This effect shows that the graded time mesh is able to resolve the non-smooth behavior of the solution induced by the right hand side.

The error for the pressure solution shows a different behavior. Due to the increased smoothness of the solution also a higher convergence order is expected for the constant time mesh. The results are presented in Fig. 5. The error plots for the constant time mesh show a nearly linear order, whereas the error for the graded time mesh shows partly a quadratic order. A super convergence behavior can be expected from the theory of Galerkin boundary element methods, which might be the reason for this high order. Again, the last point for mesh 4 gets out of the line. As already discussed, this might be an artefact of the changed

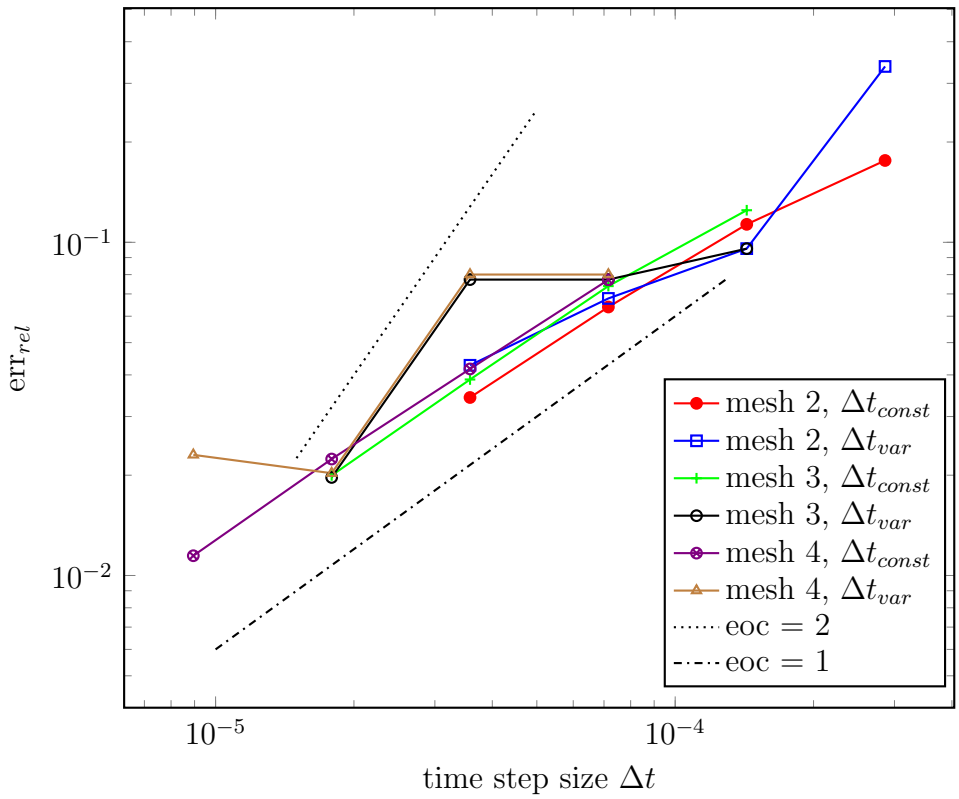

Figure 5: Relative error of the pressure versus time step size for the different meshes (double logarithmic scale)

observation time. Overall, the error plots indicate the improved behavior of the graded time mesh compared to a constant time mesh.

After studying the convergence behavior of gCQ, the influence of the admittance α is considered. In Fig. 6, the density is plotted versus time for different values of α. We employed mesh 3 for this study and have increased the observation time to $T = 0.0125223\,\mathrm{s}$. Our grading of the time mesh might be sub-optimal for the larger final time for the computation of the density since the induced "bump" is periodically repeated in the density (cf. [38]) and, in principle, would require a mesh grading also at later times. However, the intention here is to show the qualitative influence of the admittance and this might justify a sub-optimal time grading.

As expected, the increase of the admittance results in a damping of the solution and a slower decay, where the overall qualitative behavior is similar. Besides the Galerkin boundary element solution with gCQ, the analytical solution is displayed with dashed lines. Only for $\alpha = 0$ the analytical solution is omitted as it has to be derived separately. It can be observed that the numerical solution cannot follow the peaks after the first "bump". This might be improved by using a grading of the time mesh around these times and indicates that an adaptive time mesh would be advantageous. Further, for larger times the offset to the analytical solution increases. Here the limitations of a BDF 1 as underlying time discretization becomes visible. It can be expected that with a higher order method the approximation of the density becomes better and the generalization to Runge-Kutta gCQ (cf. [25]) is the topic of future research.

Interestingly, the pressure solution is not that much influenced by this deviation of the

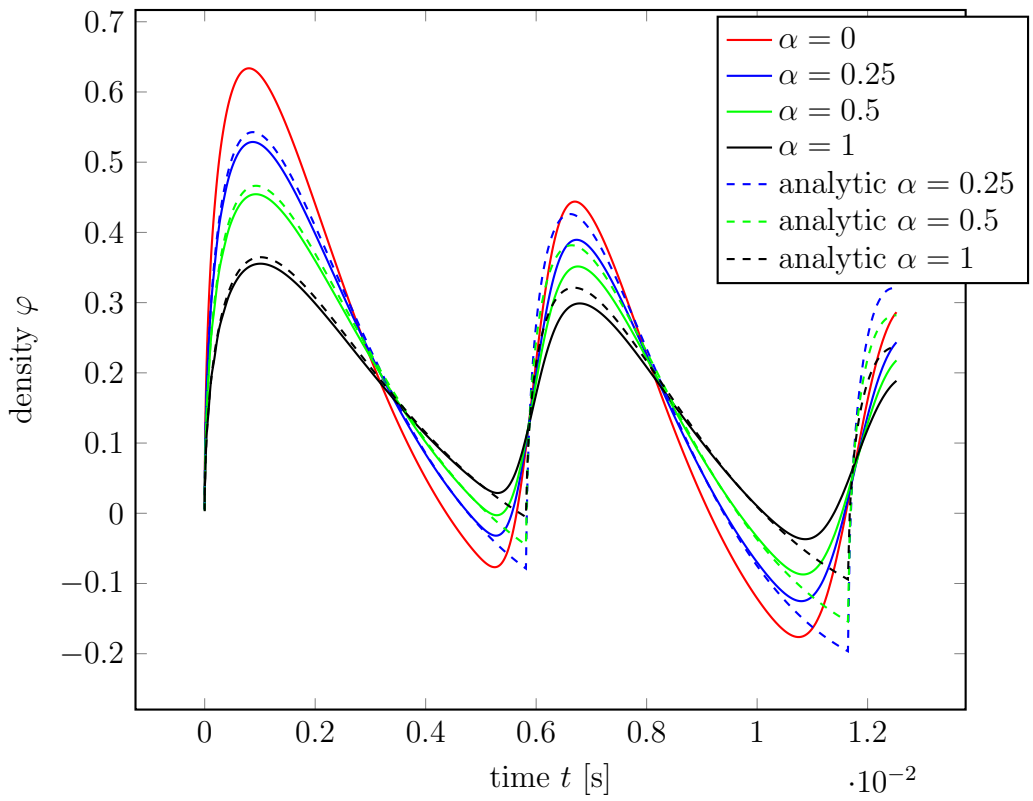

Figure 6: Density versus time for different admittances α (mesh 3)

numerical solution. In Fig. 7, the pressure is plotted versus time for the same values of α and the dots display the values of the respective analytical solution. The results match nearly perfect and the influence of the admittance is the same, it damps the solution. Theoretically this observation can be explained by the smoother behavior of the pressure compared to the density and by well known superconvergence properties of Galerkin BEM for field point evaluations. These numerical experiments confirm that the theoretical findings in Example 4.2 are sharp.

5.2 Improved acoustics in an atrium

As a realistic example the influence of absorbing layers in room acoustics is studied. In 2010/11, the atrium of the "Institut für Mathematik" at the University Zurich has been acoustically improved by installing absorber panels at the ceilings. This action has been successful and the following numerical model tries to model this effect.

The building is a cube where the offices are located in a ring around the atrium. In Fig. 8, a photo is shown from inside the atrium. On the down side of these floors sound absorbing material has been mounted. Clearly, the model does not include *every* detail of the geometry, e.g., the construction of the glas roof has not been modelled. However, the geometric model is fine enough, to model details such as the stair from the ground floor to the basement. This simplification allows to compute the sound pressure field in time domain at one node of our cluster (X4800 with 8 OctaCore-Intel CPU & 256GB RAM). This application shows that the proposed BE formulation is capable to treat real world problems.

The material data from air resulting in a wave speed $c = 343\,\mathrm{m/s}$ are assumed. Further, the

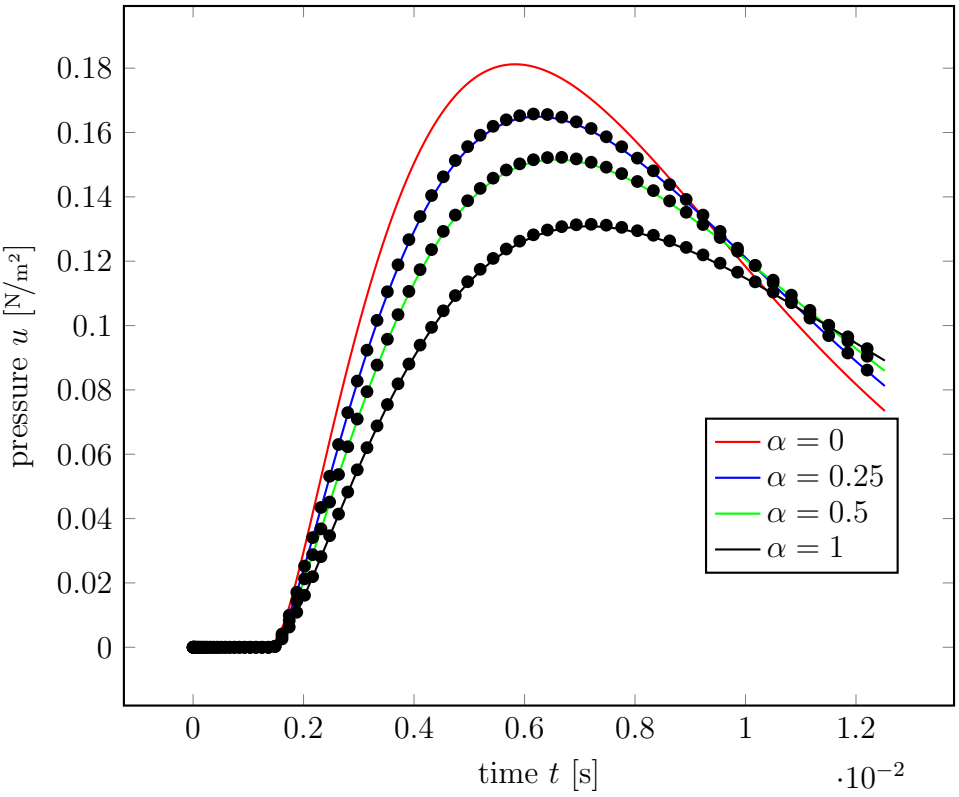

Figure 7: Pressure versus time for different admittances α (mesh 3)

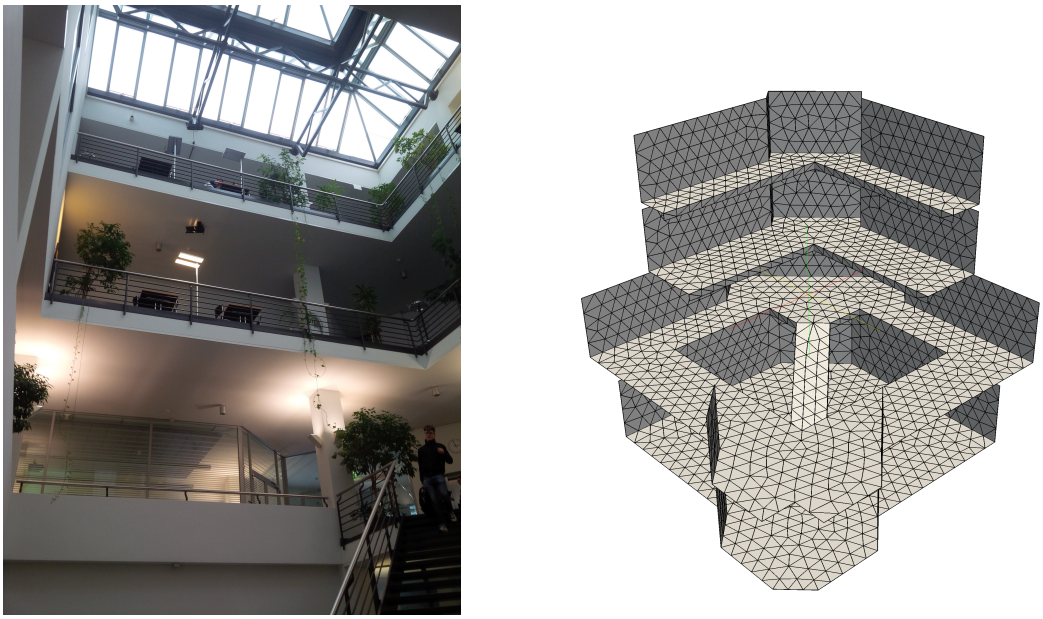

Figure 8: The atrium of the "Institut für Mathematik" at the University Zurich and the boundary element mesh. The mesh is cut such that the floors and the stair in the basement are visible.

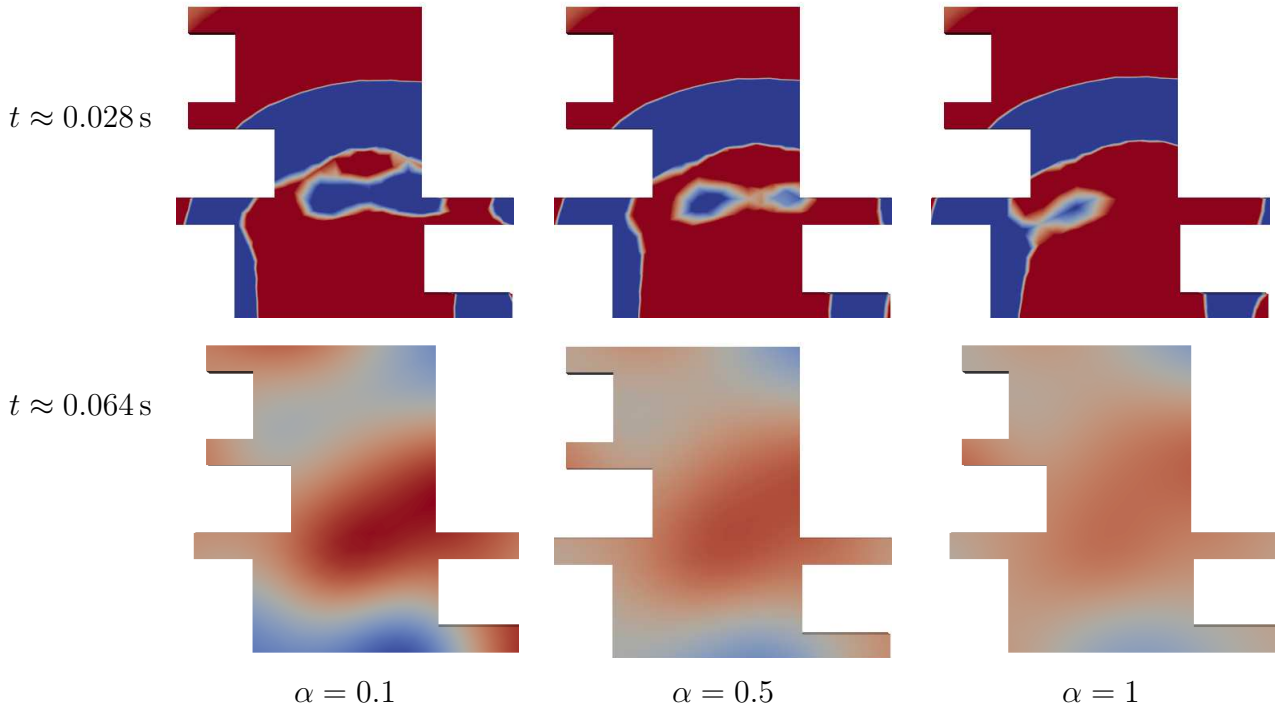

Figure 9: Sound pressure field in the atrium at different times for three different values of α

time grading is difficult to be adjusted. In contrast to the test before the solution behavior is not known in advance and would in principle require to have an adaptive algorithm. As this is subject to further research, here, a slight modification of the grading (5.1) is used. A smooth increase of time steps sizes is formulated by

$$t_n = \left(n + \frac{(n-1)^2}{N} \right) \Delta t_{const} \ , \tag{5.4}$$

which might be justified because after several reflections in this complicated geometry the solution behavior does no longer change drastically. $\Delta t_{\text{const}} = 0.00037\,\mathrm{s}$ is used to discretize the time interval $[0, T = 0.15\,\mathrm{s}]$ and $N = T/\Delta t_{\text{const}} = 405$ holds. The time grading of (5.4) results then in 248 time steps to be computed. The chosen constant time step size corresponds to $\beta \approx 0.25$. Linear continuous shape functions are employed on 7100 flat triangles[4]. The loading is a given flux at the bottom of the stairs with a time history $f(t) = \sin(1200 \cdot t)\left(H(t) - H\left(t - \frac{2\pi}{1200}\right)\right)$. This represents a sine load with $\approx 191\,\mathrm{Hz}$ active over one period. The chosen frequency represents a mean frequency of a speaking person.

In Fig. 9, the sound pressure in the atrium displayed on a screen placed nearly in the middle of the atrium is depicted for $t \approx 0.028\,\mathrm{s}$ and $t \approx 0.064\,\mathrm{s}$ for three different materials. All walls are assumed to be nearly sound hard (e.g., made of concrete with $\alpha = 0.1$) but the down side of the floors, i.e., the ceilings visible in Fig. 8 are modelled as absorbing surfaces. The chosen α-values correspond either to no sound absorbing material ($\alpha = 0.1$), to a heavy curtain at low frequencies ($\alpha = 0.5$), and to the extreme case of totally absorbing surface

[4]The geometry and the mesh have been generated by Dominik Pölz (Graz University of Technology) during his master thesis at the Institute of Applied Mechanics.

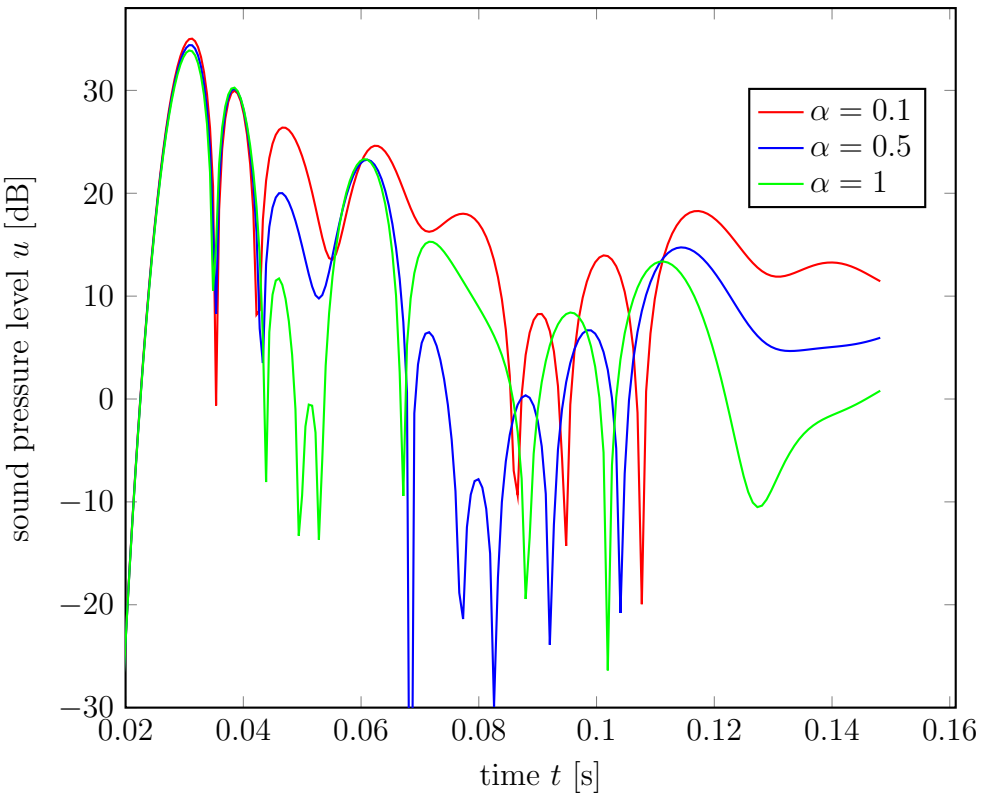

Figure 10: Sound pressure level in dB versus time in the upper left part of the observation screen

($\alpha = 1$). Note that these values are only examples and may not be the exact values for a distinct material nor the material used in reality in this atrium.

The results show clearly traveling waves in the beginning of the computation and a lot of reflections in the complicated geometry. For longer times the sound pressure level approaches a steady state with smaller values for higher damping, i.e., higher admittance. At the beginning, not much differences are visible for different values of the admittance. However, for larger observation times the sound pressure level increases as indicated by the more strong red color for the low damping material compared to the higher damping material. In Fig. 10, the sound pressure level in the upper left side of the screen is exemplarily depicted over time. Note, the sound pressure level is given in dB and negative values indicate sound below the threshold of hearing. Further, the initial phase where the pressure is zero, i.e., the time until the wave arrives, is truncated as in this case the dB measure gives very large negative values. In this plot two things can be observed. First, the peaks with the negative values show the wave reflections, which arrive for the different damping cases at different times. Second, the sound pressure for $\alpha = 0.1$, i.e. no mounted damping material, has in the mean the larger pressure values. The two other cases show that the damping material can reduce the sound pressure level as reported from the real building, where it is claimed that the atrium is no longer such noisy. Certainly, the effect is different at different locations within the atrium.

6 Conclusions

Impedance boundary conditions are very natural in acoustic calculations. They constitute a Robin type boundary condition, which can be treated easily with retarded potential integral equations. However, for impedance boundary conditions the time derivative of the Dirichlet part is combined with the Neumann part. The application of the convolution quadrature (CQ) method as time discretization for this problem is straightforward. Here, the generalized form of the CQ the gCQ is applied, which allows for a non-uniform time mesh in contrast to the original CQ method.

For a spherical scatterer, analytical solutions are derived, which are given explicitly for the scattering problem and zero order Hankel functions as spatial right-hand side. In general, the time behavior can be expressed via a time integral while, for a "bump-function", explicit expressions are presented. These solutions are used to study systematically the convergence behavior of the proposed algorithm with respect to the time discretization. The results show the expected rates. For non-smooth time behavior the gCQ is superior to a constant time mesh as expected. An open question at this point is the optimal grading of the time mesh for more general right-hand sides. Future research will elaborate on adaptivity in time, while the gCQ allows for a straightforward algorithmic realization.

Finally, a real world example has been studied. The interior sound field in the atrium of the "Institut für Mathematik"at the University Zurich has been calculated for different sound absorbing materials at the ceilings. The calculations show that the proposed method is suitable to compute such a real world application. Certainly, so-called fast methods can improve the performance of the presented formulation.

Acknowledgement The second author gratefully acknowledges the hospitality and support by the "Institut für Mathematik"at the University Zurich during his sabbatical leave.

References

[1] B. Alpert, L. Greengard, and T. Hagstrom. Rapid evaluation of nonreflecting boundary kernels for time-domain wave propagation. *SIAM J. Numer. Anal.*, 37(4):1138–1164, 2000.

[2] A. Bamberger and T. Ha-Duong. Formulation variationelle espace-temps pour le calcul par potentiel retardé d'une onde acoustique. *Math. Meth. Appl. Sci.*, 8:405–435 and 598–608, 1986.

[3] L. Banjai, C. Lubich, and J. M. Melenk. Runge-Kutta convolution quadrature for operators arising in wave propagation. *Numer. Math.*, 119(1):1–20, 2011.

[4] L. Banjai and A. Rieder. Convolution quadrature for the wave equation with a nonlinear impedance boundary condition. *ArXiv e-prints*, Apr. 2016.

[5] J. T. Beale and S. I. Rosencrans. Acoustic boundary conditions. *Bull. Amer. Math. Soc.*, 80:1276–1278, 1974.

[6] J.-P. Berenger. A perfectly matched layer for the absorption of electromagnetic waves. *J. Comput. Phys.*, 114(2):185–200, 1994.

[7] NIST Digital Library of Mathematical Functions. http://dlmf.nist.gov/, Release 1.0.9 of 2014-08-29. Online companion to [35].

[8] B. Engquist and A. Majda. Absorbing boundary conditions for the numerical simulation of waves. *Math. Comp.*, 31(139):629–651, 1977.

[9] A. Erdélyi, W. Magnus, F. Oberhettinger, and F. G. Tricomi. *Tables of integral transforms. Vol. I.* McGraw-Hill Book Company, Inc., New York-Toronto-London, 1954. Based, in part, on notes left by Harry Bateman.

[10] S. Erichsen and S. A. Sauter. Efficient automatic quadrature in 3-d Galerkin BEM. *Comput. Methods Appl. Mech. Engrg.*, 157(3–4):215–224, 1998.

[11] S. Falletta, G. Monegato, and L. Scuderi. A space-time BIE method for nonhomogeneous exterior wave equation problems. The Dirichlet case. *IMA J. Numer. Anal.*, 32(1):202–226, 2012.

[12] M. Filipe, A. Forestier, and T. Ha-Duong. A time dependent acoustic scattering problem. In *Mathematical and numerical aspects of wave propagation (Mandelieu-La Napoule, 1995)*, pages 140–150. SIAM, Philadelphia, PA, 1995.

[13] A. Franck and M. Aretz. Wall structure modeling for room acoustic and building acoustic fem simulations. In *Proc. of 19th International Congress on Acoustics*, 2007.

[14] M. Friedman and R. Shaw. Diffraction of Pulses by Cylindrical Obstacles of Arbitrary Cross Section. *J. Appl. Mech.*, 29:40–46, 1962.

[15] P. J. Graber. Uniform boundary stabilization of a wave equation with nonlinear acoustic boundary conditions and nonlinear boundary damping. *J. Evol. Equ.*, 12(1):141–164, 2012.

[16] M. J. Grote and I. Sim. Local nonreflecting boundary condition for time-dependent multiple scattering. *J. Comput. Phys.*, 230(8):3135–3154, 2011.

[17] T. Ha-Duong. On Retarded Potential Boundary Integral Equations and their Discretization. In M. Ainsworth, P. Davies, D. Duncan, P. Martin, and B. Rynne, editors, *Computational Methods in Wave Propagation*, volume 31, pages 301–336, Heidelberg, 2003. Springer.

[18] T. Ha-Duong, B. Ludwig, and I. Terrasse. A Galerkin BEM for transient acoustic scattering by an absorbing obstacle. *Int. J. Numer. Meth. Engng*, 57:1845–1882, 2003.

[19] W. Hackbusch, W. Kress, and S. Sauter. Sparse convolution quadrature for time domain boundary integral formulations of the wave equation by cutoff and panel-clustering. In M. Schanz and O. Steinbach, editors, *Boundary Element Analysis: Mathematical Aspects and Applications*, volume 18, pages 113–134. Springer Lecture Notes in Applied and Computational Mechanics, 2006.

[20] T. Hagstrom and S. I. Hariharan. A formulation of asymptotic and exact boundary conditions using local operators. *Appl. Numer. Math.*, 27(4):403–416, 1998.

[21] R. Kress. Minimizing the Condition Number of Boundary Integral Operators in Acoustics and Electromagnetic Scattering. *Q. Jl. Mech. appl. Math.*, 38:323–341, 1985.

[22] A. R. Laliena and F.-J. Sayas. Theoretical aspects of the application of convolution quadrature to scattering of acoustic waves. *Numer. Math.*, 112(4):637–678, 2009.

[23] M. Lopez-Fernandez and S. Sauter. Fast and stable contour integration for high order divided differences via elliptic functions. *Math. Comp.*, 84(293):1291–1315, 2015.

[24] M. Lopez-Fernandez and S. Sauter. Generalized convolution quadrature with variable time stepping. Part II: Algorithm and numerical results. *Appl. Numer. Math.*, 94:88–105, 2015.

[25] M. Lopez-Fernandez and S. Sauter. Generalized Convolution Quadrature based on Runge-Kutta Methods. *Numer. Math.*, 133(4):743–779, 2016.

[26] M. Lopez-Fernandez and S. A. Sauter. Generalized Convolution Quadrature with Variable Time Stepping. *IMA J. Numer. Anal.*, 33(4):1156–1175, 2013.

[27] C. Lubich. Convolution quadrature and discretized operational calculus I. *Numer. Math.*, 52:129–145, 1988.

[28] C. Lubich. Convolution quadrature and discretized operational calculus II. *Numer. Math.*, 52:413–425, 1988.

[29] C. Lubich. On the multistep time discretization of linear initial-boundary value problems and their boundary integral equations. *Numer. Math.*, 67:365–389, 1994.

[30] C. Lubich. Convolution quadrature revisited. *BIT Numerical Mathematics*, 44:503–514, 2004.

[31] C. Lubich and A. Ostermann. Runge-Kutta methods for parabolic equations and convolution quadrature. *Math. Comp.*, 60(201):105–131, 1993.

[32] M. Messner, M. Messner, F. Rammerstorfer, and P. Urthaler. Hyperbolic and elliptic numerical analysis BEM library (HyENA). `http://www.mech.tugraz.at/HyENA`, 2010. [Online; accessed 22-January-2010].

[33] L. Nagler, P. Rong, M. Schanz, and O. v. Estorff. Sound transmission through a poroelastic layered panel. *Comput. Mech.*, 53(4):549–560, 2014.

[34] J. C. Nédélec. *Acoustic and Electromagnetic Equations*. Springer, New York, 2001.

[35] F. W. J. Olver, D. W. Lozier, R. F. Boisvert, and C. W. Clark, editors. *NIST Handbook of Mathematical Functions*. Cambridge University Press, New York, NY, 2010. Print companion to [7].

[36] S. Sauter and A. Veit. A Galerkin Method for Retarded Boundary Integral Equations with Smooth and Compactly Supported Temporal Basis Functions. *Numer. Math.*, 123:145–176, 2013.

[37] S. Sauter and A. Veit. Retarded Boundary Integral Equations on the Sphere: Exact and Numerical Solution. *IMA J. Numer. Anal.*, 34(2):675–699, 2013.

[38] S. Sauter and A. Veit. Adaptive Time Discretization for Retarded Potentials. *Numer. Math.*, 132(3):569–595, 2016.

[39] F.-J. Sayas. *Retarded Potentials and Time Domain Boundary Integral Equations: A Road Map*. Springer Verlag, 2016.

[40] E. P. Stephan, M. Maischak, and E. Ostermann. Transient Boundary Element Method and Numerical Evaluation of Retarded Potentials. In M. Bubak, G. van Albada, J. Dongarra, and P. Sloot, editors, *Computational Science – ICCS 2008, LNCS, 5102*, pages 321–330, Heidelberg, 2008. Springer.

[41] J. Stratton. *Electromagnetic Theory*. McGraw-Hill, New York, 1941.

[42] A. Veit. *Numerical Methods for Time-Domain Boundary Integral Equations*. PhD thesis, Inst. f. Math., Universität Zürich, 2012.